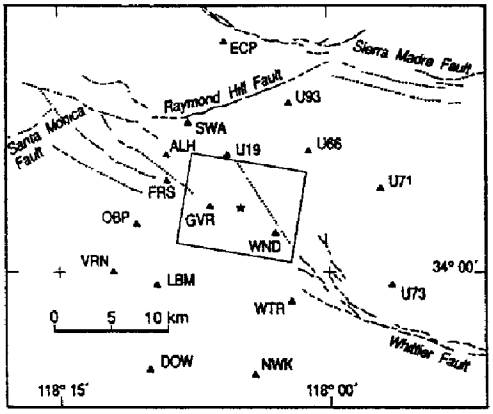

Fig. 1 Area map showing the locations of the strong motion stations used in this study and the surface projection or map view of the model fault plane indicated by the rectangular box. The epicenter is indicated by the star.

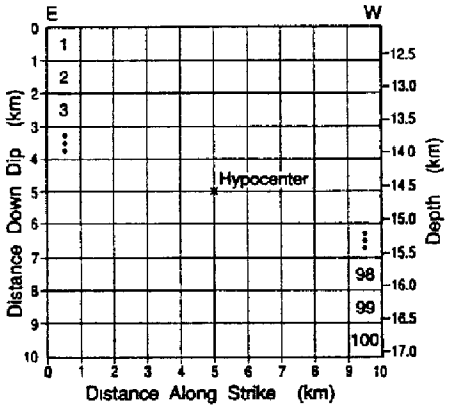

Fig. 2 Parametrization of the model fault plane used in the inversion of the strong motion records. The fault is subdivided into 1 km^2 subfaults for which the model parameters dip-slip dislocation, strike-slip dislocation, and rupture time are calculated.

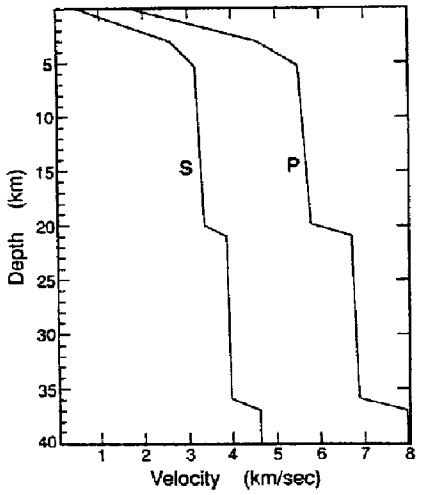

Fig. 3 Velocity structure used to calculate ground motion at the strong motion sites. The most important feature of the model is the large velocity gradient near the surface.

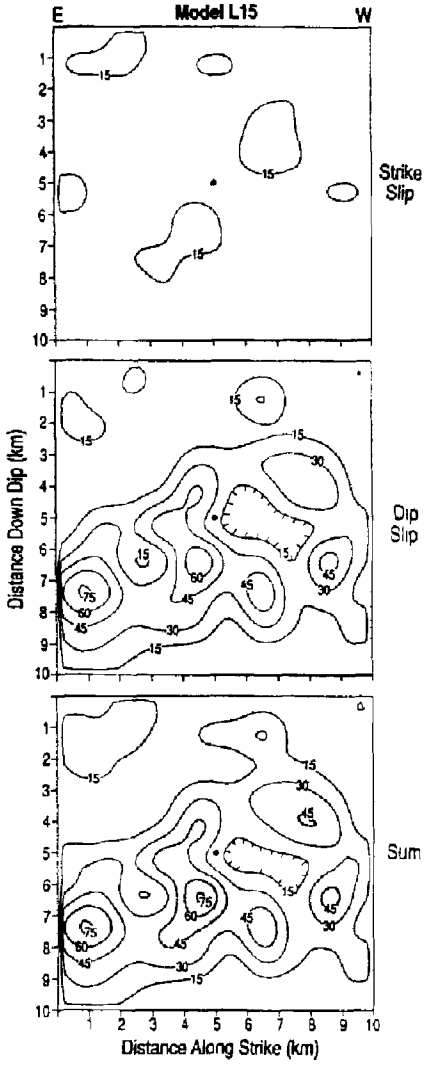

Fig. 4 Contours of slip in centimeters for model L15. In this model each subfault ruptures once at a constant rupture velocity of 2.5 km/s.

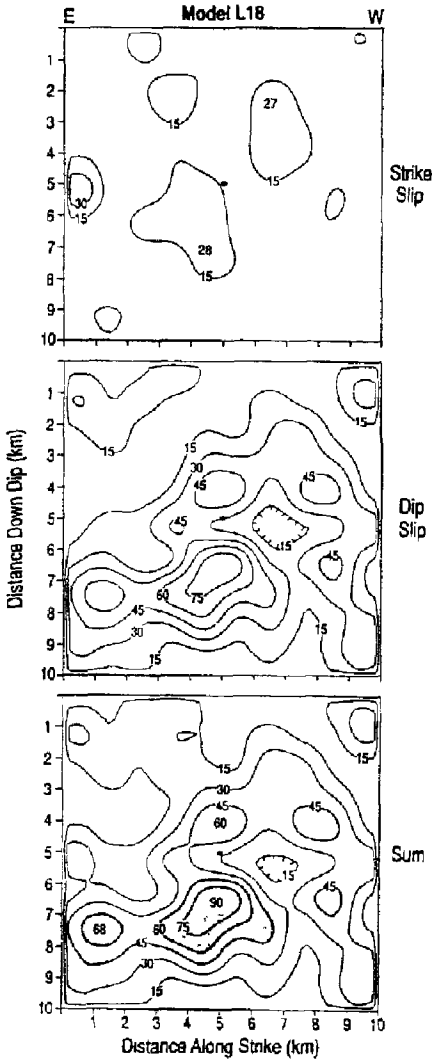

Fig. 5 Contours of slip in centimeters for model L18. In this model each subfault is allowed to rupture twice to allow for a more complex source-time function. The rupture velocity is fixed at 2.5 km/s.

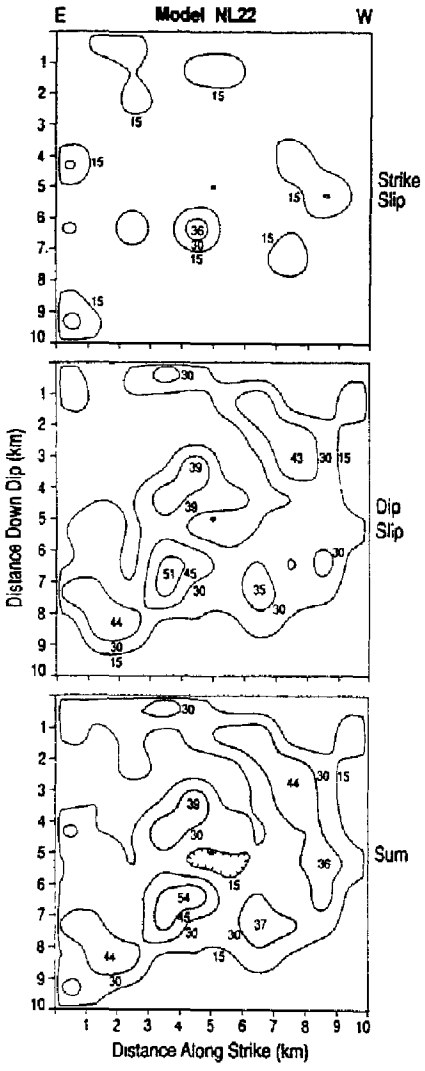

Fig. 6 Contours of slip in centimeters for model NL22 In this model each subfault ruptures once, but the rupture velocity is not fixed, and the rupture times for each subfault are free to vary

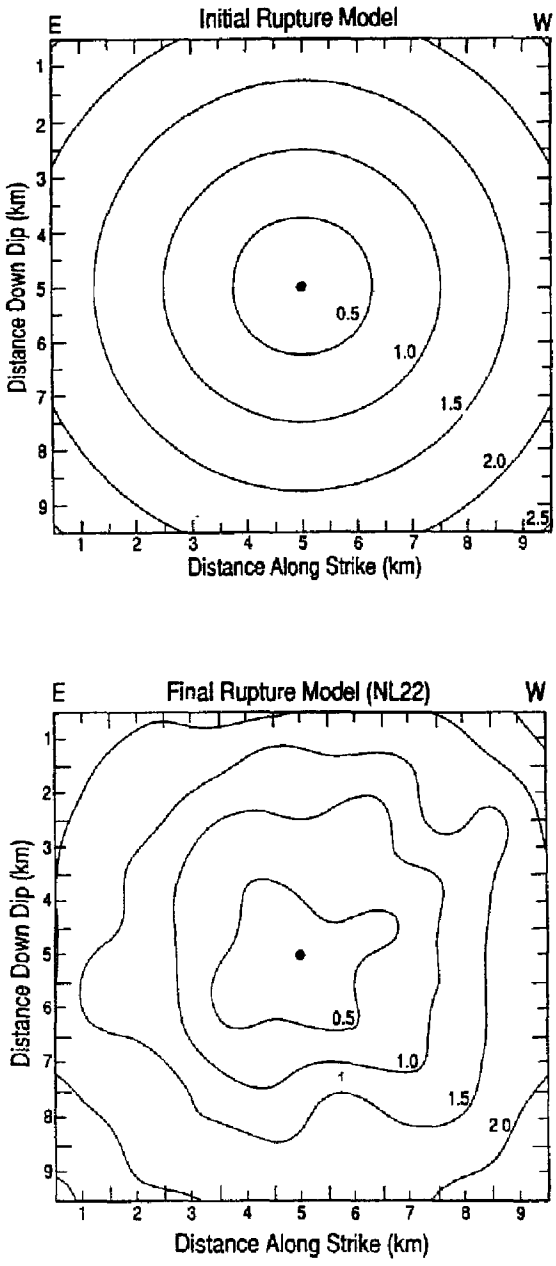

Fig. 7 Contours of the initial and final rupture times for model NL22. The starting rupture model is a constant velocity of 2.5 km/s.

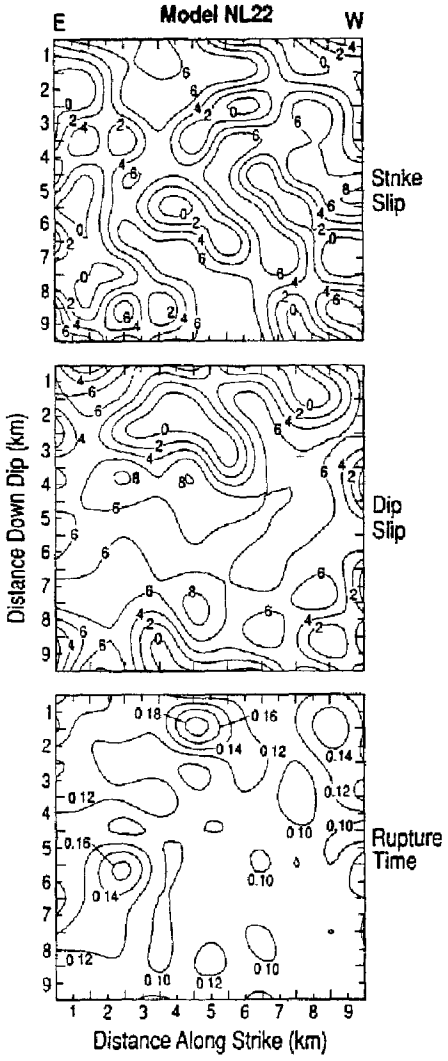

Fig. 8 Contours of model perturbations δx from equation (6) for model NL22 assuming a data tolerance of 1.0. Areas with zero values correspond to regions where the model parameters are identically zero.

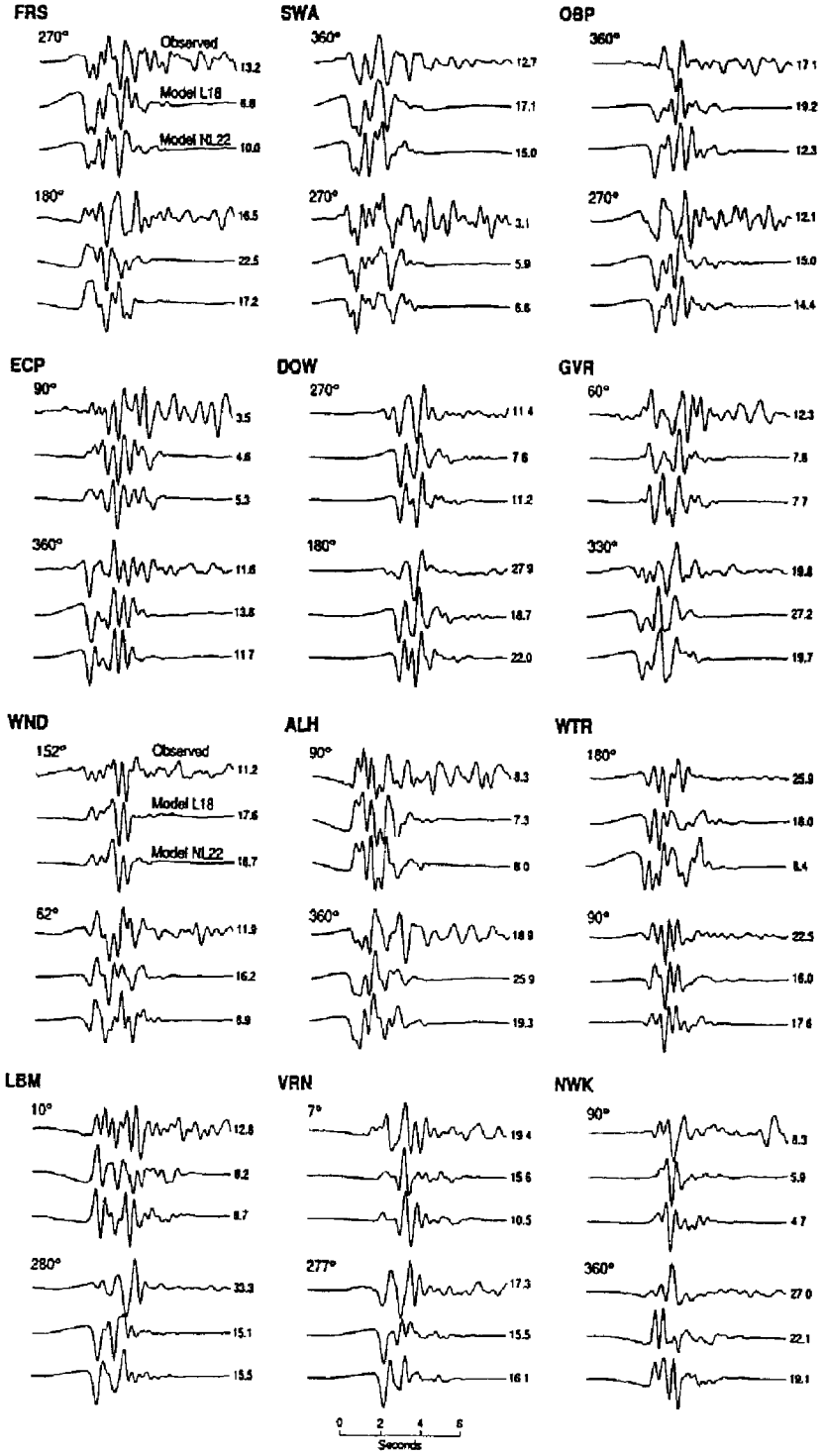

Fig. 9 Comparison of the observed strong motion velocity records (first trace) with the synthetic ground motion records for models L18 (second trace) and NL22 (third trace).

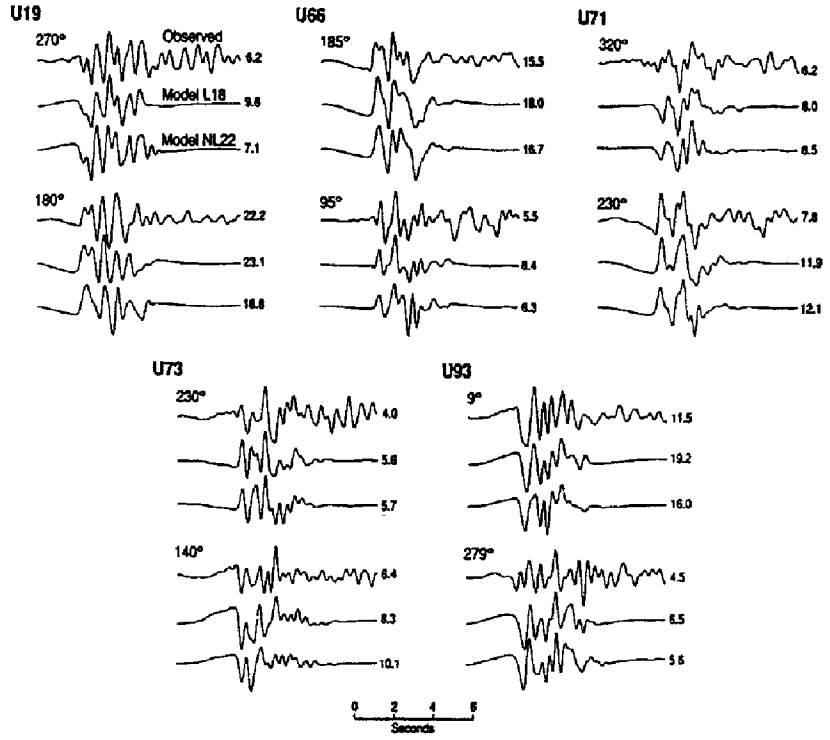

Fig. 9 (continued)

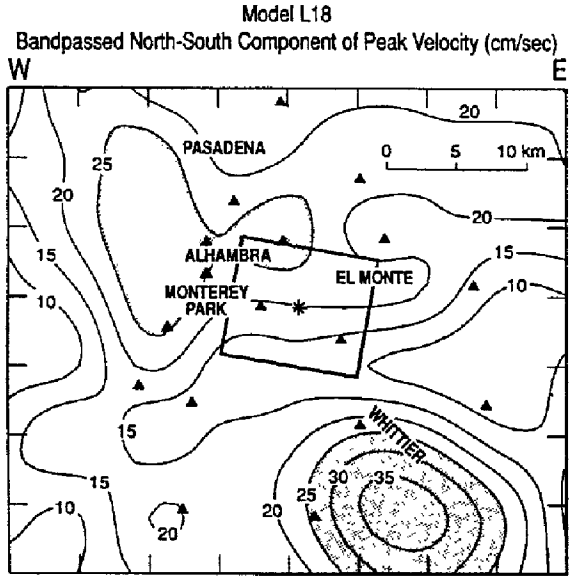

Fig. 10 Predicted peak velocities for model L18 in the passband 0.2 to 3.0 Hz. Values contoured are the peak whole record velocities for the north-south component of motion.

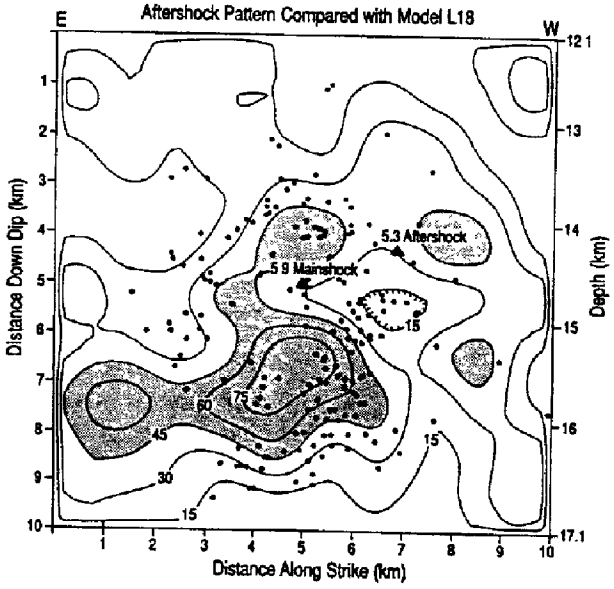

Fig. 11 Comparison of a perpendicular projection of the aftershock locations onto the model fault plane with the slip from model L18. The aftershocks occurred in a ring pattern approximately coincident with a low in the slip distribution.

Lecture 1 SOURCE INVERSION

Subject 2 Source Inversion of High-Frequency Strong Motion Records in the Near-Source Region

1. INTRODUCTION

Probably, the best way to understand the nature of high-frequency strong seismic ground motion is interpretation of the whole strong-motion waveform. It has been undoubtedly verified by numerous studies that high-frequency strong motion is heavily affected by local effects near the station, including soil nonlinear behavior. For example, this situation was summarized by Aki [1]. Recently, we come to recognize that source effect, path effect, and site effect jointly affect strong-motion seismograms. This might be exemplified by the 1985 Michoacan, Mexico earthquake (e.g., [2]). Considering these situations, one of the most controversial topics is source effects which are related to damage and intensity patterns even in the high-frequency range. Importantly, source effects of an earthquake influence all the observation stations. Near-source records which are not much influenced by local site effects should be analyzed to minimize propagation path effects.

2. GENERAL SOURCE INVERSION

The most effective way to investigate source effects for a large earthquake is to perform a source inversion for the retrieval of the temporal behavior of slip on an extended fault. An elast-dynamic representation theorem is used in order to relate the dislocation across the fault surface to the radiated elastic field. The discretization of the representation theorem leads to a system of linear equations relating the unknown slip distribution vectors with the recorded ground motion data vectors, through a matrix of the Green's functions for the medium.

Trifunac's [3] formulation established a basic methodology of modern source inverse problems. In his study, the prescribed fault plane was divided into a small number of subfaults. Ground motion from each subfault was calculated using the Haskell model [4], which gives a synthetic displacement in an infinite homogeneous medium. A least-squares fit to displacement time histories was used to determine slip on each subfault on the condition that the hypocenter location and the rupture mode were prescribed.

Physically reasonable constraints were added to the Trifunac's formulation in order to obtain the practical, spatio-temporal characteristics of the inferred slip on the fault plane [5, 6]. The constraints include (a) linear smoothing constraints to stabilize the solutions and (b) positive constraints on the solutions to obtain positive dislocation. The third constraint is (c) minimum constraints on the solutions to uniquely define which solutions are to be chosen

Different types of formulations are an iterative deconvolution method [7], a frequency-domain inversion method [8], and a differential array analysis [9]. In the iterative deconvolution method, constituent events of a multiple shock sequence are determined one by one in the decreasing order of the event size using an iterative procedure with a least-squares criterion. This method seems to work well in the cases of large earthquakes with separate concentrations of slip in the low-frequency range. The frequency-domain inversion method has an advantage that performing the temporal deconvolution in the frequency domain allows the spatial dependence of slip to be computed independently at each frequency. This greatly reduces the computational effort and allows the grid spacing to be chosen sufficiently fine. The differential array analysis is suitable for high frequencies, which are very difficult to process in usual source inversion frameworks. The technique makes use of a difference in arrival

---

* This lecture note is based on the paper of the same title written by Masahiro Iida and Stephen Hartzell, published on "IUTAM (International Union Theoretical Applied Mechanics), Symp. Inverse Problems Eng. Mechanics, pp. 393-401, Tokyo, Japan, May 1992".

times of distinguishable phases in body-wave seismograms obtained from a source region. Recently, non-linear inversion methods of determining an optimal location of the rupture front are being developed (e.g., [10, 11]).

3. HIGH-FREQUENCY SOURCE INVERSION

The suitable way to estimate source effects in the high-frequency range seems to treat a system of linear equations with physically reasonable constraints, as Olson and Apsel [5] or Hartzell and Heaton [6] performed. The first reason is that reliable solutions are expected over the whole fault plane because of linear smoothing and positive constraints. Secondly, since the whole fault plane is subdivided into a large number of subfaults, the rupture process can be analyzed in detail. Thirdly, this method has been applied to many earthquakes with actual velocity models, confirming the effectiveness of the method. However, source effects that are closely related to damage and intensity patterns have not been demonstrated although some studies have been conducted in the high-frequency range. The most likely reason is luck of well-instrumented earthquakes. Also, detailed damage and intensity patterns have not been surveyed in most earthquakes.

We apply a modified version of Hartzell and Heaton's method [6] to the 1987 Whittier Narrows, California, earthquake, one of the best instrumented earthquakes to date [11]. We note the unusual damage and intensity patterns of this earthquake [12] (Fig. 1); In other words, Whittier, which is not located in the source area, experienced the greatest damage. Also, the northwestern side of the fault had more damage than the surrounding areas. Such patterns could not be interpreted by only local site effects [13].

The pattern of 17 near-source stations that form good azimuthal coverage of the source is expected to give good resolution (Fig. 1) [14, 15]. To minimize propagation path effects, only station within 15 km of the epicenter are used. With this cutoff, the station ranges are comparable to or less than the source depths, which emphasizes the direct body waves. Only horizontal components are used, which are dominated by S wave energy. Band-pass filtered velocity records from 0.2 to 3.0 Hz are used. This frequency range is responsible for much of an earthquake's damage and intensity.

4. INVERSION METHOD

Our inversion method was discussed in detail by Hartzell and Iida [11], and is roughly reviewed here. The model fault is a square planar region 10 km on an edge. We fix the strike of our model fault at 280°. Two different values of dip, 30° and 40° were tried, and a dip of 30° gave a marginally better fit to the data. The hypocenter is located at the center of the fault plane at a depth of 14.6 km. The fault plane is divided up into small square regions of equal area. Each subfault is 1 km^2. The Green's function that includes all theoretical arrivals is calculated for each subfault and station pair, using the discrete wave number/finite element method of Olson *et al.* [16], which is applicable to a 1-dimensional velocity gradient model. The velocity model is characterized by slow surface velocities of steep gradients in the upper 5 km, typical of the Los Angeles basin. Actually, a cross section of the basin does not show uniform underground structure horizontally [17]. Although no local effects are taken into account, abnormal site effects are not recognized as far as we visually inspect the seismograms.

If we wish to solve for the slip amplitudes for a prescribed rupture velocity, the problem is linear. The observed records and the subfault synthetic records then form an overdetermined system of linear equations,

$$A\ x \cong b$$

where A is the matrix of synthetics, b is the data vector, and x is the solution vector of the subfault dislocation weights. Because instability of the solution arises, the problem is stabilized by appending linear constraints giving

$$\begin{pmatrix} Cd^{-1}A \\ \lambda_1 S \\ \lambda_2 M \end{pmatrix} x \cong \begin{pmatrix} Cd^{-1}b \\ 0 \\ 0 \end{pmatrix}$$

S is a matrix of smoothing constraints. M is a matrix of minimization constraints λ_1 and λ_2 are linear weights. Cd is an a priori data covariance matrix. The solution vector is solved for using a Householder reduction method that invokes a positivity constraint on the solution [18]. If we wish to solve simultaneously for the magnitude of the slip and the rupture initiation time for each subfault, the problem is nonlinear and is solved in an iterative manner We then have an overdetermined problem which is solved using a least squares criterion for a model parameter perturbation vector.

Three different types of waveform inversion are performed. The first and simplest approach assumes a constant rupture velocity with each subfault rupturing once. The second formulation also uses a fixed rupture velocity, but each subfault is allowed to rupture twice with a small time interval, to allow for a more complex source-time function. The third type of inversion allows each subfault to rupture once, but the rupture velocity, in other words, the rupture time of each subfault may vary.

5. IMPLICATIONS OF HIGH-FREQUENCY INVERSION

The slip distributions for the three rupture models are shown in Fig. 2. They indicate a complex rupture process within a small source volume, with at least four separate concentrations of slip. The data records are compared with the synthetics for the second and third rupture models in Fig 3. The waveforms are fit well in both shape and amplitude, especially at the earlier parts of the records. The same tendency was recognized in previous inversion studies [5, 6, 10]. We should note that the large-amplitude sections are not influenced so much by local site effects. the later parts of the records most likely contain propagation path effects not included in our simple model. The underground structure in the Whittier Narrows region is not horizontally uniform [17]. Therefore, Iida and Spudich are developing a scatterer inversion to explain the later phases seen at observed seismograms [19].

In order to interpret the unusual damage and intensity patterns for the Whittier earthquake, the ground motion in the epicentral region is predicted on the basis of the inferred distribution of slip. The result for the model (b) of Fig. 2 is shown at the lower-left corner of Fig. 1, where peak velocities are contoured. It is consistent with the intensity and damage distributions; The area of highest expected velocities is near the town of Whittier. The second largest amplitudes are to the west and northwest of the epicenter. The results of this study indicate that the ground motion in the source region can be explained by considering source effects coupled with the same averaged propagation path effects to each strong motion station.

6. REFERENCES

[1] Aki, K. (1988). Local site effects on strong ground motion, *Proc. Earthq. Eng. Soil Dynamics II -- Recent Advances in Ground Motion Evaluation*, 103-155, Park City, Utah, USA.

[2] Campillo, M., J.C. Gariel, K. Aki and F.J. Sanchez-Sesma (1989). Destructive strong ground motion in Mexico City: Source, path and site effects during great 1985 Michoacan earthquake, *Bull Seism. Soc Am.*, **79**, 1718-1735.

[3] Trifunac, M.D. (1974). A three-dimensional dislocation model for the San Fernando, California, earthquake of February 9, 1971, *Bull. Seism. Soc. Am.*, **64**, 149-172.

[4] Haskell, N.A. (1969). Elastic displacements in the near-field of a propagation fault, *Bull. Seism. Soc. Am.*, **59**, 865-908

[5] Olson, A H. and R.J. Apsel (1982). Finite faults and inverse theory with applications to the 1979 Imperial Valley earthquake, *Bull. Seism. Soc. Am.*, **72**, 1969-2001.

[6] Hartzell, S.H. and T.H. Heaton (1983). Inversion of strong motion and teleseismic waveform for the fault rupture history of the 1979 Imperial Valley, California, earthquake, *Bull. Seism. Soc. Am.*, **73**, 1553-1583.

[7] Kikuchi, M. and H. Kanamori (1982). Inversion of complex body waves, *Bull. Seism. Soc. Am.*, **72**, 491-506.

[8] Olson, A.H. and J.G Anderson (1988). Implications of frequency-domain inversion of earthquake ground motions for resolving the space-time dependence of slip on an extended fault, *Geophysical Journal*, **94**, 443-455.

[9] Spudich, P. and E. Cranswick (1984). Direct observation of rupture propagation during the 1979 Imperial Valley earthquake using a short baseline accelerometer array, *Bull. Seism. Soc Am.*, **74**, 2083-2114.

[10] Beroza, G.C. and P. Spudich (1988). Linearized inversion for fault rupture behavior: Application to the 1984 Morgan Hill, California, earthquake, *J. Geophys. Res.*, **93B**, 6275-6296.

[11] Hartzell, S. and M. Iida (1990). Source complexity of the 1987 Whittier Narrows, California, earthquake from the inversion of strong motion records, *J. Geophys. Res.*, **95B**, 12475-12485.

[12] Leyendecker, E.V., L.M. Highland, M. Hopper, E.P. Arnold, P. Thenhaus and P. Powers (1988). The Whittier Narrows, California earthquake of October 1, 1987 -- Early results of isoseismal studies and damage surveys, *Earthquake Spectra*, **4**, 1-10.

[13] Kawase, H. and K. Aki (1990). Topography effect at the critical SV wave incidence: Possible explanation of damage pattern by the Whittier Narrows, California earthquake of October 1, 1987, *Bull. Seism. Soc. Am.*, **80**, 1-22.

[14] Iida, M., T. Miyatake and K. Shimazaki (1988). Optimum strong-motion array geometry for source inversion, *Earthq. Eng. Struct Dyn.*, **16**, 1213-1225.

[15] Iida, M. (1990). Optimum strong-motion array geometry for source inversion -- II, *Earthq. Eng. Struct. Dyn.*, **19**, 35-44.

[16] Olson, A.H., J. Orcutt and G. Frazier (1984) The discrete wavenumber/finite element method for synthetic seismograms, *Geophys. J.R. Astron. Soc.*, **77**, 421-460.

[17] Davis, T.L., J. Namson and R.F. Yerkes (1989). A cross section of the Los Angeles area: Seismically active fold and thrust belt, the 1987 Whittier Narrows earthquake, and earthquake hazard, *J. Geophys. Res* , **94B**, 9644-9664.

[18] Lawson, C. and R. Hanson (1974). Solving least squares problems, Prentice-Hall, Englewood Cliffs, N.J.

[19] Iida, M. and P. Spudich (1992). Scatterer inversion based on microearthquake seismograms, *Proc. Int. Symp. Effects Surface Geology Seismic Motion I*, 239-244, Odawara, Japan.

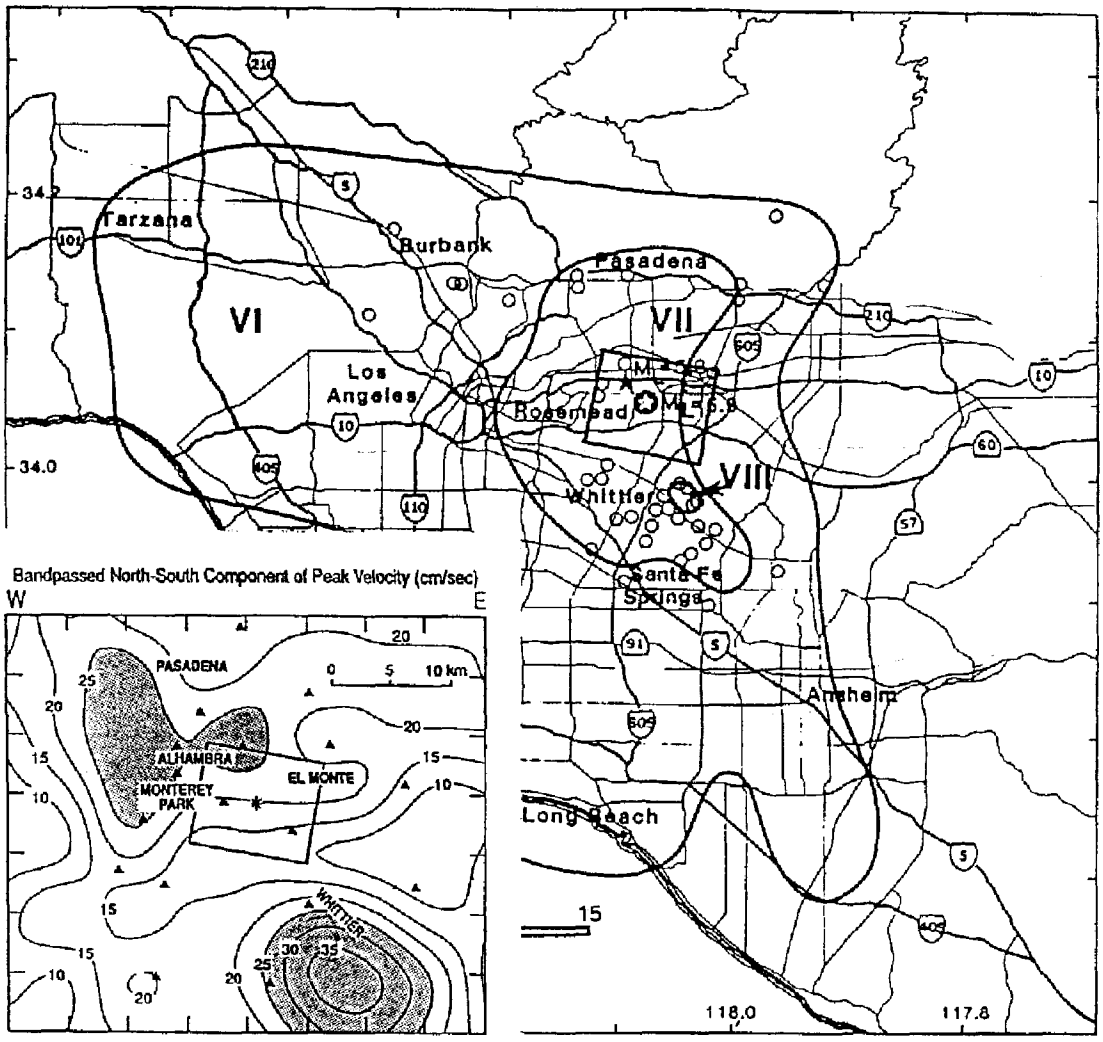

Fig. 1 Regional Modified Mercalli intensity isoseismals of the Los Angeles area in the earthquake of October 1, 1987. The surface projection of the model fault plane is indicated by the rectangular box. Open circles represent the center of the census tracts surveyed. The circled star is the main shock epicenter (After Leyendecker *et al.*). Predicted peak velocities (cm/sec) for the model (b) of Fig. 2 in the bandpass 0.2 to 3.0 Hz are shown on the same scale at the lower left corner. Values contoured are peak whole record velocities in the north-south component of motion. The stations used are indicated by solid triangles.

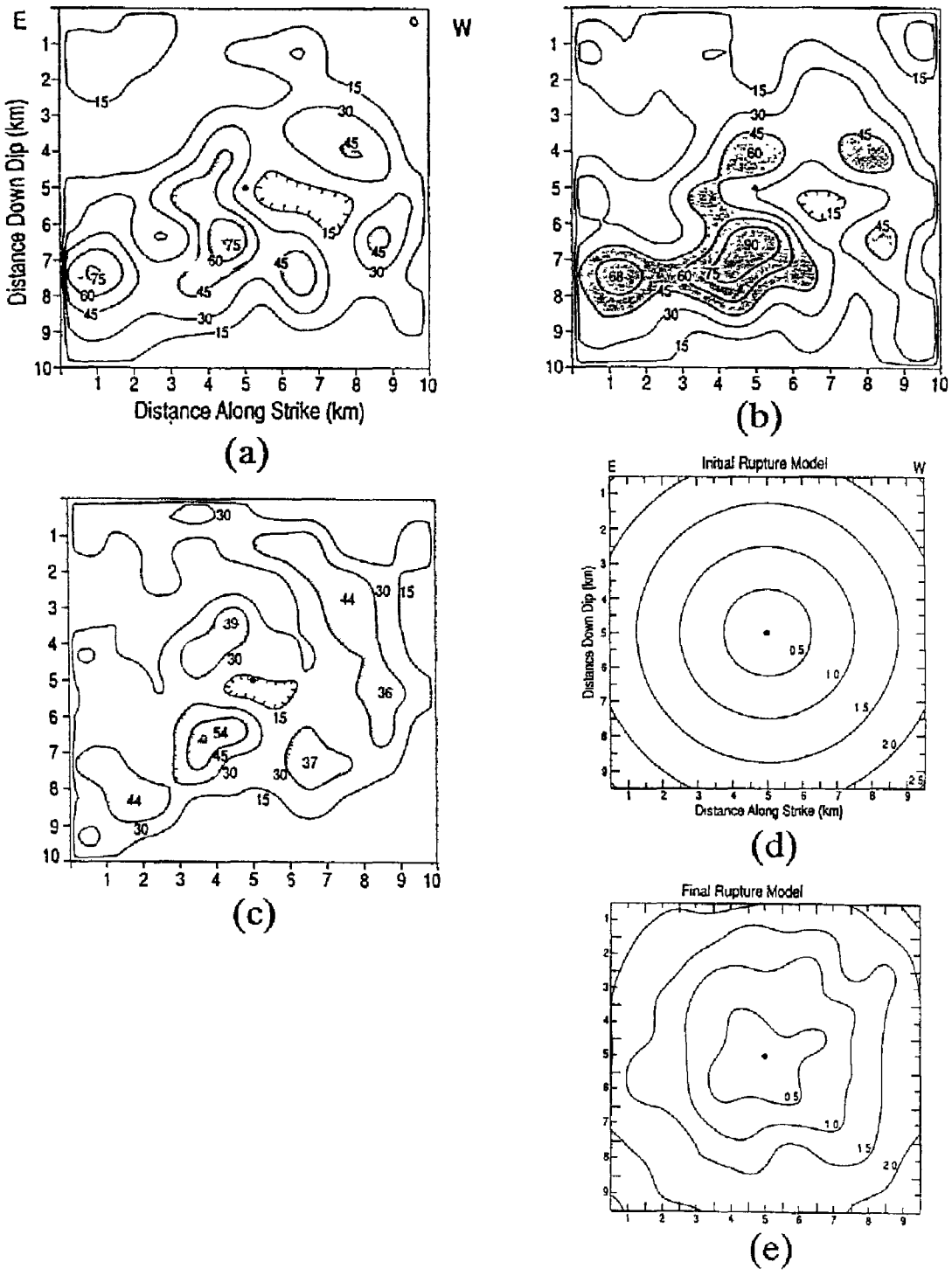

Fig. 2 Contours of slip in centimeters. (a) Each subfault ruptures once at a constant rupture velocity of 2 5 km/s. (b) Each subfault is allowed to rupture twice with a certain small time interval in order to allow for a more complex source-time function. The two ruptures progress at a fixed speed of 2.5 km/s. The rupture mode of (a) and (b) is shown in (d). (c) Each subfault ruptures once, but the rupture time for each subfault is free to vary. Starting with the initial rupture mode of (d), the final rupture mode of (e) is obtained.

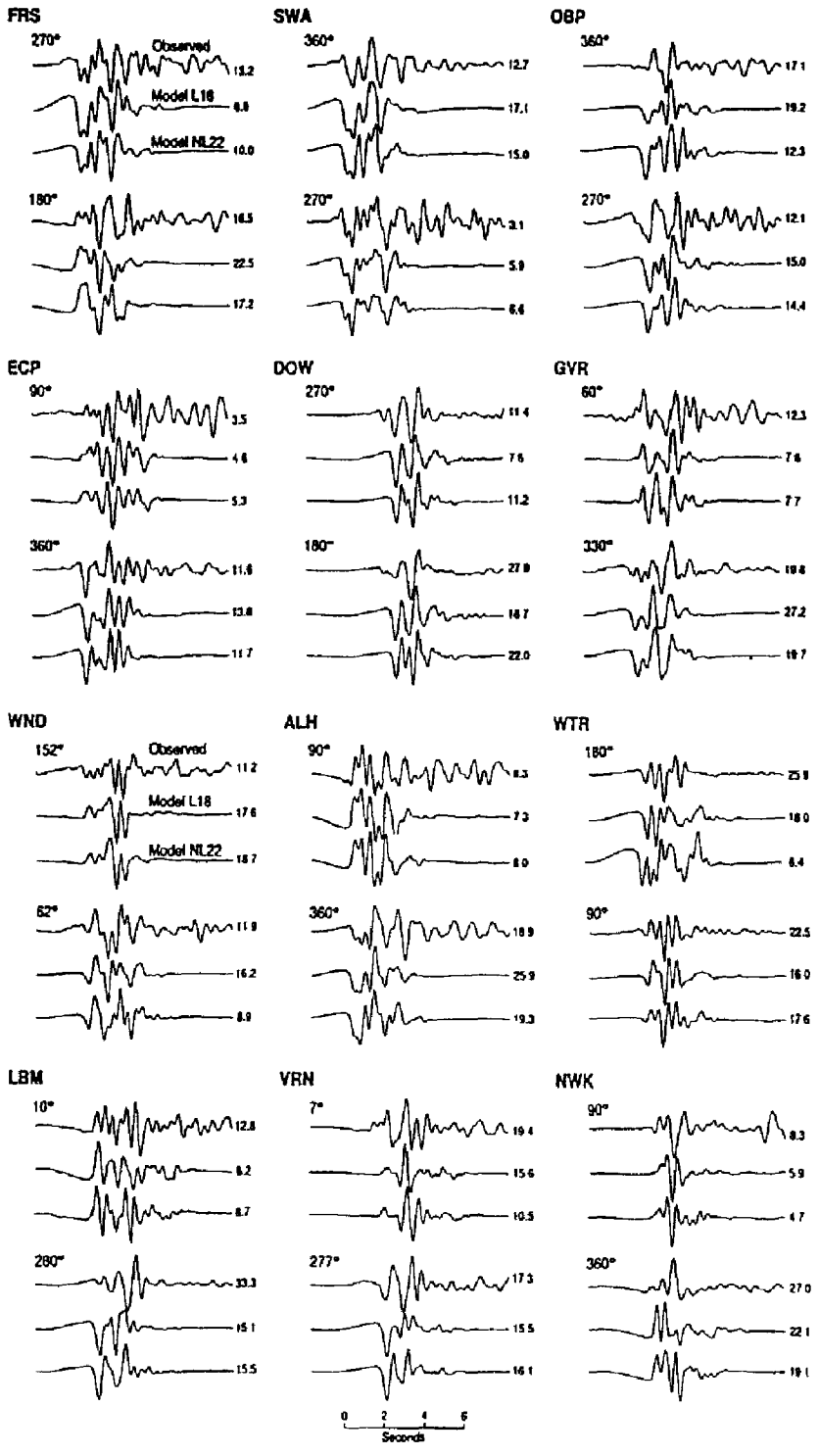

Fig. 3 Comparison of the observed strong-motion velocity records (first trace) with the synthetic ground motion records for the model (b) (second trace) and the model (c) (third trace) of Fig. 2.